Research Article

Nanomedicine

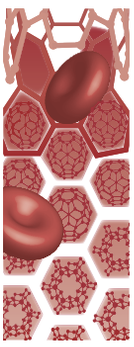

Calcium carbonate nanoparticles stimulate tumor metabolic reprogramming and modulate tumor metastasis

Avik Som[‡,1,2], Ramesh Raliya[‡,3], Krishna Paranandi[1], Rachel A High[4], Nathan Reed[3], Scott C Beeman[1], Matthew Brandenburg[1], Gail Sudlow[1], Julie L Prior[1], Walter Akers[1,5], Annelise Y Mah-Som[6], Lemoyne Habimana-Griffin[1,2], Joel Garbow[1], Joseph E Ippolito[1,7], Mark D Pagel[4], Pratim Biswas[3] & Samuel Achilefu*[,1,2,8,9]

[1]Mallinckrodt Institute of Radiology, Washington University in St Louis School of Medicine, St Louis, MO 63110, USA
[2]Department of Biomedical Engineering, Washington University in St Louis, St Louis, MO 63130, USA
[3]Department of Energy, Environmental, Chemical Engineering, Washington University in St Louis, St Louis, MO 63130, USA
[4]Cancer Biology Graduate Interdisciplinary Program, University of Arizona Cancer Center, Tucson, AZ 54724, USA
[6]Department of Pediatrics, Division of Rheumatology, Washington University in St Louis School of Medicine, St Louis, MO 63110, USA
[5]Center for *In Vivo* Imaging & Therapeutics, St. Jude Children's Research Hospital, Memphis, TN 38105, USA
[7]Department of Genetics, Washington University in St Louis School of Medicine, St Louis, MO 63110, USA
[8]Department of Medicine, Washington University in St Louis School of Medicine, St Louis, MO 63110, USA
[9]Department of Biochemistry & Biophysics, Washington University in St Louis School of Medicine, St Louis, MO 63110, USA
*Author for correspondence: Tel.: +1 314 362 8599; achilefu@wustl.edu
[‡]Authors contributed equally

Aim: $CaCO_3$ nanoparticles (nano-$CaCO_3$) can neutralize the acidic pHe of solid tumors, but the lack of intrinsic imaging signal precludes noninvasive monitoring of pH-perturbation in tumor microenvironment. We aim to develop a theranostic version of nano-$CaCO_3$ to noninvasively monitor pH modulation and subsequent tumor response. **Materials & methods:** We synthesized ferromagnetic core coated with $CaCO_3$ (magnetite $CaCO_3$). Magnetic resonance imaging (MRI) was used to determine the biodistribution and pH modulation using murine fibrosarcoma and breast cancer models. **Results:** Magnetite $CaCO_3$-MRI imaging showed that nano-$CaCO_3$ rapidly raised tumor pHe, followed by excessive tumor-associated acid production after its clearance. Continuous nano-$CaCO_3$ infusion could inhibit metastasis. **Conclusion:** Nano-$CaCO_3$ exposure induces tumor metabolic reprogramming that could account for the failure of previous intermittent pH-modulation strategies to achieve sustainable therapeutic effect.

First draft submitted: 20 August 2018; Accepted for publication: 6 November 2018; Published online: 6 December 2018

Keywords: magnetite • MRI • nano-$CaCO_3$ • pH modulation • theranostic

Effective cancer therapy remains difficult because of significant side effects and off-target toxicity associated with common approaches such as chemotherapy [1] and radiotherapy [2]. Further complications arise from the development of resistance as tumor cells undergo mutations and adaptive reprogramming to escape therapy. Recent studies have shown that the tumor microenvironment plays important roles in cancer growth and metastasis. As a result, interest in developing therapies that can modulate the extracellular milieu and avoid development of therapeutic resistance has intensified. For example, one such target is the relatively acidic extracellular pH of many solid tumors. Cancer cells utilize aerobic glycolysis to fuel their growth (Warburg metabolism), synthesizing lactic acid from glucose in the presence or absence of oxygen. Efflux of the excess lactic acid and protons via various mechanisms decreases the extracellular pH (pHe = 6.8) of solid tumors relative to the physiologic pHe in tissues (pHe 7.2–7.4) [3,4] and this process has been noted as a hallmark of cancer [5,6]. Low pHe activates matrix degradation enzymes to facilitate metastasis and inactivates some chemotherapeutics. Thus, targeting or modulating the pHe of tumors can improve drug-delivery via pH-responsive nanoparticles [7,8] or cell-penetrating peptides [9]. Neutralizing tumor acidity can also directly inhibit growth and metastasis via selective proton pump

Future Medicine

inhibitors [10], bicarbonate infusions [11] or nanoparticle-based buffering [12]. Recent studies have also found that changing tumor extracellular pH synergizes with other therapies, including chemotherapy [13,14], anti-angiogenesis therapy [15], radiation therapy [16] and immunotherapy [10].

Of these methods used to change pHe, $CaCO_3$ nanoparticles (nano-$CaCO_3$) have been particularly effective due to their high payload and buffering capacity, allowing them to deliver drugs [7,17] and directly modulate the local pHe [12] in acidic environments, respectively. Recent studies have shown that formation of albumin coronal shell stablizes most forms of $CaCO_3$ crystalline forms *in vivo*. Changing their crystalline properties can confer different degrees of dissolution [18]. Biocompatiblity of diverse calcium-based nanoparticles has favored their use in the diagnosis and treatment of diseases [19]. In particular, the strong buffering capacity of nano-$CaCO_3$ compared with microparticle versions makes them particularly attractive for *in vivo* applications [18–20]. These materials have a low potential for side effects, as they degrade into calcium (regulated by the kidney and deposited into the bone) and CO_2 (exhaled by the lungs), and only increases the pHe to a maximum of 7.4 [12], the normal physiologic pH of most healthy tissues. As a result, nano-$CaCO_3$ provides buffering when needed but does not induce alkalosis, even at high concentrations. We previously reported tumor inhibition in a fibroasarcoma xenograft murine model with daily administration of nano-$CaCO_3$, associated with a pH increase that reversed upon ceasing administration of the nano-$CaCO_3$ [12]. The effect of nano-$CaCO_3$ is not dependent on inhibiting any specific acid secretion pathway, avoiding traditional drug resistance via genetic mutation. However, we have not yet assessed pHe changes after clearance of nano-$CaCO_3$, or its effect, if any, on tumor glycolytic metabolism.

Despite recent progress in the therapeutic applications of nano-$CaCO_3$, it has been difficult to determine the biodistribution of nano-$CaCO_3$ and noninvasively map subsequent pH changes *in vivo*. This handicap reduces our ability to optimize its therapeutic potential. Unlike some nanoparticles, such as gold and silver nanoparticles, nano-$CaCO_3$ does not have an intrinsic signaling moiety to track *in vivo* distribution. Nanoparticle-derived calcium and carbonate are difficult to differentiate from endogenous ions. The conventional approach to directly incorporate imaging moieties such as fluorescent dyes or radionuclides into the nanoparticle's surface is less applicable to nano-$CaCO_3$ because the imaging component will dissociate from the bulk nanoparticles as they dissolve *in vivo*. Coating the surface of the nano-$CaCO_3$ with polymers or other materials that provide linkage groups for conjugation of imaging agents alters the highly pH-controlled $CaCO_3$ release that sets these particles apart from other pH modulators. Although radioactive calcium could be used, this approach presents challenges on several levels, including the use of dedicated synthesis room and apparatus, as well as the costs associated with the disposal of long-lived radioisotopes. For these reasons, there are no reports of imaging nano-$CaCO_3$ distribution *in vivo*.

In this study, we synthesized magnetite encapsulated by nano-$CaCO_3$, (magnetite $CaCO_3$ [m-$CaCO_3$]) for detection by MRI. MRI has been used to image magnetite nanoparticle distributions *in vitro* and *in vivo* [21,22]. We correlated biodistribution with changes in pHe and glucose uptake measured through acido-chemical exchange saturation transfer (acidoCEST)-MRI and 18F-fluorodeoxyglucose (FDG) positron emission tomography (PET). Additionally, we developed a proof-of-concept nano-$CaCO_3$ therapy for metastasis inhibition. Thus, m-$CaCO_3$ serves as a theranostic, with both diagnostic and imaging uses as well as therapeutic potential. In the process, we discovered that nano-$CaCO_3$ induces tumor metabolic reprogramming, unique among nanoparticles.

Materials & methods

Synthesis of nano-$CaCO_3$

This method has been previously published [12]. $CaCl_2$ hexahydrate (100 mg; 0.46 mmol; Sigma–Aldrich, Saint Louis, MO, USA) was dissolved in anhydrous ethanol (50 ml) in a 400 ml beaker in a desiccator containing with drierite. The beaker was surrounded by 16 glass vials (20 ml) filled with ammonium bicarbonate (typically 20 g per vial) and placed under vacuum for 1–3 days with completion determined by a change in the turbidity of the solution with a visual change to a light blue, cloudy solution. The volume was reduced by approximately 10 ml ethanol during the reaction. The solid nanoparticles were then isolated from the ethanol solution by centrifuging at 6800 × *g* for 10 min in 1 ml Eppendorf tubes, then air dried. The resultant solid was recombined in fresh ethanol and resuspended by sonication, followed by storage at room temperature. Yield was determined by sampling 10 ml of the resultant solution, and weighing the dry mass.

Synthesis of m-$CaCO_3$

Monodisperse iron oxide nanoparticles (IONPs; magnetite) were synthesized by thermal decomposition of iron carboxylate $Fe(CO)_5$ at high temperature. In a typical synthesis of 15 nm iron oxide nanoparticles, a mixture of

2 mmol FeO(OH) fine powder and 2 mmol oleic acid in 5.0 g of 1-octadecene was heated and stirred under argon atmosphere at 320°C. The reaction proceeded for 2 h before cooling to room temperature. The suspension was purified with a standard washing procedure using hexane and acetone, then dispersed in hexanes. The purified particles were transferred from hexane to water by ligand addition of sodium monododecyl phosphate using sonication. During this process, 0.5 ml of IONPs in hexane solution and 1 mM sodium monododecyl phosphate were added to 10 ml of ultrapure water in a glass vial. The mixture of organic and aqueous phase was then ultra-sonicated for 20 min. After sonication, the brown suspension was heated to 70°C for 1 h to evaporate residual hexane. The IONPs were further purified via ultracentrifugation (Sorvall WX Ultra 80, Thermo Scientific, MA, USA), filtration through a syringe filter (pore size of 0.2 um, Millipore) and redispersion by sonication [23]. A premixed solution of $CaCl_2 \bullet 2H_2O$ (0.1 M) and $NaHCO_3$ (0.1 M) in water and ethylene glycol (1:5 v/v; Sigma–Aldrich) were dispersed in the aqueous dispersion of monodisperse IONPs and mixed at room temperature. The synthesized m-$CaCO_3$ particles were collected by sequential wash with ethanol, methanol and acetone, as reported previously, and stored as a dry powder at room temperature [12,20].

Transmission electron microscope

Transmission electron microscope (TEM) micrographs were obtained using an FEI Spirit TEM (OR, USA) operated at 120 kV. A 400-mesh Formvar carbon-coated copper grid was glow-discharged in a vacuum evaporator (Denton, NJ, USA) for 30 s. The sample was prepared by placing 2 µl of sonicated $CaCO_3$ nanoparticles solution onto the grid and wicking off the excess sample with filter paper after 30 s. The grid left to dry out at room temperature before TEM analysis.

x-ray diffraction

x-ray diffraction (XRD) patterns were obtained by using the Bruker d8 Advance x-ray diffractometer (Bruker, MA, USA) configured with a Cu x-ray tube with 1.5418 Å for analysis of powder samples using LYNXEYE_XE detector. For the analysis, fine ground $CaCO_3$ nanoparticles were kept on a Zero diffraction plate (MTI Corporation, CA, USA). XRD data were scanned from 20–60 degrees, with a 0.04 degree step size, a 0.5 s per step count time, with sample rotation turned on (15 r.p.m.), and with a coupled two-theta/theta scan. The Bruker Diffrac. Eva program was used for the evaluation and processing of XRD scan data. Search-match operations included search by diffraction index list, by name, using chemistry filters and via an International Centre for Diffraction Data (ICCDD PDF) database filter to confirm crystal type.

Hydrodynamic diameter & electro-kinetic zeta potential

To study agglomeration kinetics of $CaCO_3$ nanoparticles, the hydrodynamic diameter was measured using time-resolved dynamic light scattering (Malvern Instruments, MA, USA). The zeta potential was measured using a Malvern zetasizer nano ZS instrument. An applied voltage of 100 V was used for the analyses. A minimum of three measurements was made per sample.

Animal studies & tumor models

All animal studies were conducted in compliance with Washington University and Arizona University Animal Welfare Committees' requirements for the care and use of laboratory animals in research. BALB/c and athymic nu/nu mice were purchased from Frederick Cancer Research and Development Center. HT1080 tumors were generated by subcutaneous injection of 4×10^6 cells in 100 µl of Dulbecco's phosphate-buffered saline (PBS) into the dorsal flanks of athymic nu/nu mice. Likewise, MDA-MB-231 tumors were generated by injecting MDA-MB-221 cells into the dorsal flanks of BALB/c mice or by tail vein injection. 4T1 tumors were generated by injection of 4×10^5 cells in 100 µl of PBS into the mammary fat pads of BALB/c mice or 1×10^6 cells intravenously via tail vein.

Phantom imaging of m-$CaCO_3$ nanocomposite

Eighty-one milligram of m-$CaCO_3$ particles were suspended in 1 ml of 2% (v/v) bovine serum albumin (BSA) in Dulbecco's PBS supplemented with $MgCl_2$ and $CaCl_2$, and then serially diluted five times, each time by a factor of 10 in 2% BSA–PBS. The resulting 1 ml solutions (81, 8, 0.8, 0.08 and 0.008 mg/ml) were placed in microcentrifuge tubes and imaged by a 7T Biospec MRI scanner (Bruker Biospin, Inc., MA, USA). The transverse

relaxation rate constant (R_2) was measured for each dilution using a Carr-Purcell-Meiboom-Gill type spin-echo pulse sequence by employing 12 echo times ranging from 13 to 300 ms and a repetition time of 2 s.

In vivo imaging of m-$CaCO_3$

Mice bearing tumors between 1.0 and 1.5 cm in diameter were injected with 1 mg w/v m-$CaCO_3$ via tail vein. Each mouse was anesthetized, secured to a customized cradle, inserted into a 7T Biospec MRI scanner (Bruker Biospin, Inc.) and measured using the Carr-Purcell-Meiboom-Gill sequence described above. The mouse's breathing rate was monitored and the core body temperature was regulated at 37.0 ± 0.5°C. Depending on the tumor model, measurements were taken pre-injection, immediately postinjection and after 1, 2, 4–6, and 24 h postinjection. The transverse relaxivity of the particle (r_2) was calculated based on the linear relation (assuming low concentrations of particles) between R_2 and particle/iron concentration:

$$R_{2,obs} = R_{2,0} + r_2\,[NP],$$

where $R_{2,obs}$ is a measured transverse relaxation rate constant; $R_{2,0}$ is the calculated transverse relaxation rate constant in the absence of the nanoparticle, also referred as the 'background' R_2; and [NP] is the nanoparticle concentration. Images were analyzed in MATLAB (Mathworks, Inc., MA, USA).

18F-Fluorodeoxyglucose positron emission tomography

BALB/c mice bearing HT1080 tumors were shaved and injected intravenously with FDG at 5 mCi/kg dose. FDG activity was measured by PET over a 60 min tumor uptake study after overnight fasting. Mice were then injected with 1 mg of nano-$CaCO_3$ in 100 µl of 2% murine serum albumin in PBS and allowed to feed again before an overnight fast. At approximately 24 h post-nano-$CaCO_3$ administration, mice were again injected with FDG and then measured for PET activity over 60 min.

AcidoCEST-MRI pH measurements *in vivo*

AcidoCEST protocol has been previously described [24–26]. Briefly, each mouse was anesthetized, catheterized and secured to a customized cradle, and inserted into the MRI machine. A bolus of 200 µl of iopromide was injected via the catheter, followed by infusion of iopromide at 400 µl/h for the duration of imaging. A respiration-gated CEST-FISP (fast imaging with steady state precession) MRI protocol acquired images with 54 saturation frequencies using 2.8 µT saturation power and a saturation period of 5 s. This CEST MRI protocol was repeated four times before injection and six times after injection, for a total time of approximately 55 min. The acidoCEST magnetic resonance imaging (MRI) images were processed with MATLAB R2012B (Mathworks, Inc.), as previously described [24–26].

Continuous infusion of nano-$CaCO_3$

In BALB/c mice bearing mammary fat pad 4T1luc-GFP tumors, bioluminescence imaging (BLI) was performed using the IVIS Lumina System (Perkin Elmer, MA, USA) to estimate tumor size on day 1 after implantation. Nano-$CaCO_3$ (3 mg) was suspended in EtOH (200 µl) along with cypate (100 µM in ethanol 100 µl). The mixture was placed in a Lynch coil connected to an Alzet osmotic pump (Model 2004, DURECT Corporation, CA, USA) with a 28-day infusion time (0.15 µl/h). The pump was implanted on day 2 post-tumor implantation and connected via a catheter into the jugular vein. Animals rested for 2–3 days after surgery. On day 6, nano-$CaCO_3$ (1 mg) in 100 ul 2% BSA–PBS was injected intravenously, and the animals were imaged by BLI the same day as well as approximately every 4 days up to day 30. To detect lung metastasis, the primary tumor was covered with a black material and a long exposure was taken of the chest region. Control mice were implanted with tumors but not osmotic pumps.

For extravasation experiments requiring intravenous (iv.) injection of tumor cells, pumps were similarly implanted. Three days after pump implantation, nano-$CaCO_3$ (1 mg) was injected via tail vein, followed 3–5 min later by 4T1luc-GFP cells. The mice were imaged by BLI at 2 h and then days 2, 6, 9 and 13 days after iv. tumor injection before being euthanized.

Determination of toxicity in cells

HT1080 fibroadenoma cells were grown to near-confluency in a 96 well plate. The cells were plated in a 96-well plate and incubated with m-$CaCO_3$ nanoparticles at various concentrations from 0 to 1.2 mg/ml for 24 h, under

Iscove's Modified dulbecco's medium media (pH 7.4). The sulforhodamine B assay [27] was used to determine the cytotoxicity, which was expressed as a percentage of viable cells relative to the untreated control. Each condition was plated with four technical replicates.

Determination of toxicity in rats

Three month old Sprague Dawley rats (n = 6; 2 females and 4 males) were used to determine the *in vivo* toxicity of m-$CaCO_3$ nanoparticles. The nanoparticles were dispersed in 2% w/v rat serum albumin in PBS supplemented with $CaCl_2$ and $MgCl_2$. The 2% (v/v) m-$CaCO_3$ nanoparticles were injected with an allometrically dosed 25.4 mg/kg of a stock solution (30 mg/ml), approximately equivalent to a 40 mg/kg mouse injection reported previously [12]. As a control, six rats (n = 6; 3 females and 3 males) were injected with a vector of 2% rat serum albumin–PBS using an equivalent volume (1.333 ml/kg) as in the treated group. Toxicity was then analyzed by histology, complete blood count, white blood cell differential and a basic metabolic panel.

Statistical methods

Statistics were calculated using Prism (GraphPad, CA, USA) for Kaplan–Meier log rank tests, and Microsoft Excel (Microsoft, WA, USA) for two tailed t-tests.

Data availability

Underlying raw data are available on request.

Results

Synthesis & characterization of m-$CaCO_3$

Magnetite (iron oxide) nanoparticles were synthesized by thermal decomposition of iron carboxylate purified, and then mixed with $CaCl_2$ hexahydrate and sodium bicarbonate in water and ethylene glycol to form m-$CaCO_3$ nanoparticles. TEM micrographs of m-$CaCO_3$ demonstrated a characteristic spherical shape and size range (100 $\pm$ 8.5 nm) of the particles dispersed in methanol (Figure 1A). The images show the integration of the magnetite particles into the nano-$CaCO_3$ as dark spots of the appropriate size (inset of Figure 1A). XRD patterns clearly showed that both nano-$CaCO_3$ and m-$CaCO_3$ were vaterite crystals (Figure 1B). The images clearly show the composite of nano-$CaCO_3$ alone (Supplementary Figure 1) and magnetite (Supplementary Figure 2). The known ratio of presynthesized magnetite nanoparticles added to the final product of m-$CaCO_3$ matched well with the final concentration of iron measured by Inductively coupled plasma mass spectrometry (ICP-MS) analysis.

Stability of m-$CaCO_3$ in aqueous medium is achieved with an albumin solution

Using time-resolved dynamic light scattering, the stability of both nano-$CaCO_3$ and m-$CaCO_3$ were determined in a variety of solvents including water, saline, BSA, DMEM, ethanol, methanol and PBS. The m-$CaCO_3$ shared similar stability as nano-$CaCO_3$ in 2% albumin/PBS or DMEM, with both solutions providing the greatest stability and least aggregation over time (Figure 1C & D). In contrast, water and saline destablized the particles, probably due to rapid equilibration or ion exchange.

Imaging of nano-$CaCO_3$ distribution *ex vivo* & *in vivo* using m-$CaCO_3$ in a fibrosarcoma xenograft murine model

Incorporation of magnetite allowed the use of MRI to image $CaCO_3$ nanoparticles *in vitro* and *in vivo*. Phantom imaging of *in vitro* solutions demonstrated the ability to detect a sample of m-$CaCO_3$ at 0.1 mg/ml, a 100-fold dilution from normal injection doses of 1 mg in 100 µl for nano-$CaCO_3$ (Figure 2A). Accumulation of m-$CaCO_3$ in fibrosarcoma HT1080 tumors *in vivo* caused a decrease in T_2 relaxation time (increase in R_2 or $1/T_2$), which appeared first in the kidney, then liver and finally tumor (Figure 2B). Images of liver and kidney obtained during the experiment are shown in Supplementary Figure 3.

The T_2 signal throughout the animal decreased rapidly with a trough at around 6 h, followed by the return of signal approaching the original T_2 profile by 24 h (Figure 2C). The significant reduction of T_2 in the bladder suggests a substantial component of renal clearance, whereas T_2 recovery in the tumor indicates that m-$CaCO_3$ is dissolving in the tumor's acidic pH as designed and the free magnetite is clearing from the tissue (Figure 2C). Subsequent studies were conducted with nano-$CaCO_3$, except where m-$CaCO_3$ was used for imaging the particles' distribution *in vivo*.

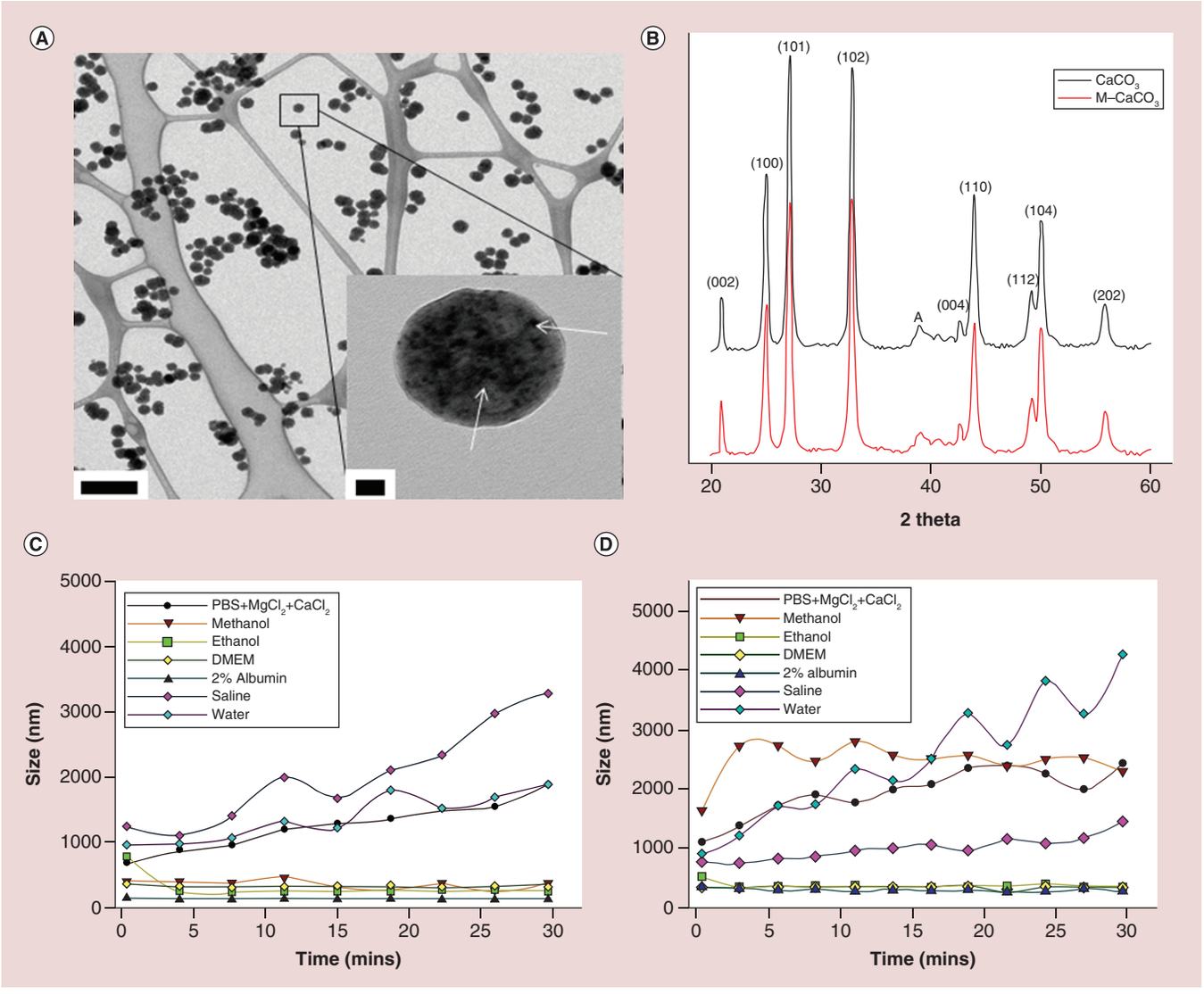

Figure 1. Characterization of magnetite $CaCO_3$. (A) Transmission electron microscope images of m-$CaCO_3$ particles when dispersed in methanol (scale bar 500 nm). Inset in **(A)**: higher magnification of the m-$CaCO_3$ particles (scale bar of 20 nm). The black dots indicated by arrows within the bulk of the $CaCO_3$ particle are the magnetite nanoparticles. **(B)** x-ray diffraction characterization of nano-$CaCO_3$ (black) and m-$CaCO_3$ (red) composite shows vaterite composition for both m-$CaCO_3$ and nano-$CaCO_3$. **(C)** Stability test of nano-$CaCO_3$ in various solvents measured by time-resolved dynamic light scattering over 30 min. **(D)** Stability test of m-$CaCO_3$ in various solvents measured by time-resolved dynamic light scattering. For both particle types, the order of stability is 2% albumin > ethanol = DMEM > saline > PBS + $MgCl_2$ > methanol > water.
m-CaCO3: Magnetite $CaCO_3$; Nano-$CaCO_3$: $CaCO_3$ nanoparticles; PBS: Phosphate-buffered saline.

Measuring metabolic reprogramming in the fibrosarcoma model

HT1080 tumor-bearing mice were treated with nano-$CaCO_3$, and glucose metabolism was measured by uptake of the glucose analog FDG using PET. FDG signal in tumors 24 h after nano-$CaCO_3$ introduction showed a statistically significant reduction in glucose uptake in the tumor ($p = 0.046$, 2-tailed paired t-test), but with no change in the muscle ($p = 0.69$; Figure 2D). This finding was true for total FDG uptake by the tumor (area under the curve, Figure 2E) and at each time point post-FDG administration (Figure 2F). This reduction was localized primarily to the tumor and not the muscle (Figure 2G).

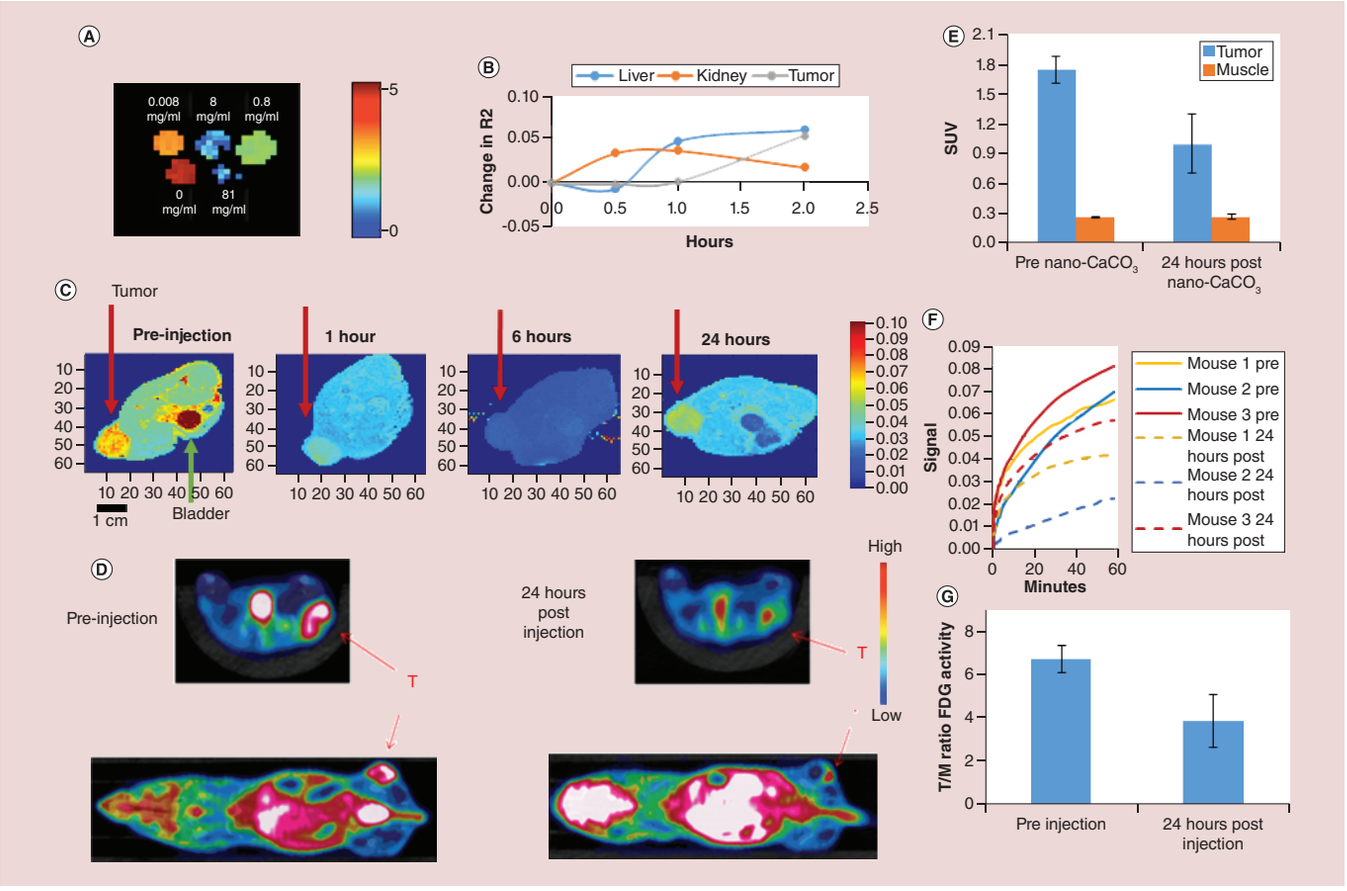

Figure 2. Analysis of *in vivo* $CaCO_3$ nanoparticles penetration in fibrosarcoma HT1080 xenografts and subsequent metabolic changes. **(A)** *Ex vivo* phantom imaging using magnetic resonance imaging of magnetite-CaCO3 (m-$CaCO_3$) at different concentrations (0.008–81 mg/ml range). Increase in m-$CaCO_3$ concentration leads to a reduction in T_2. Scale is T_2. For **(B & C)**, m-$CaCO_3$ was administered to HT1080 tumor-bearing mice intravenous injection. **(B)** Change in R_2 ($1/T_2$) over time in the liver, kidney and HT1080 tumor after injection of m-$CaCO_3$, representative profile. **(C)** Visualization of T_2 changes with m-$CaCO_3$ injection in a cross section of a mouse (representative images of n = 3 mice). Red arrow shows tumor, green arrow shows the mouse's bladder. Note the drop in T_2 throughout, with recovery by 24 h. Heat map shows relative T_2, with red and blue indicating high and low activity, respectively. For **(D–G)**, HT1080 tumor-bearing mice were given a tail vein injection of $CaCO_3$ nanoparticles (nano-$CaCO_3$) and imaged using FDG-PET (n = 3 mice). **(D)** Representative PET activity heat maps in cross section of a mouse at 0 and 24 h after nano-$CaCO_3$ injection. White is beyond threshold, red arrow (T) indicates tumor. **(E)** Tumor versus muscle uptake of FDG, area under the curve over 1 h. **(F)** Difference in FDG uptake pre- and post-nano-$CaCO_3$ administration over the course of glucose uptake. Pretreatment (solid lines); 24 h post-treatment (dashed lines). **(G)** Comparison of FDG tumor/muscle ratio.
FDG: 18F-Fluorodeoxyglucose positron; m-$CaCO_3$: Magnetite CaCO3; Nano-CaCO3: $CaCO_3$ nanoparticles; PET: Positron emission tomography.

MRI-derived pH measurement of tumors with $CaCO_3$ nanoparticles in breast cancer murine models

For imaging the biodistribution of particles, we investigated m-$CaCO_3$ in a subcutaneous xenograft model of human breast cancer (MDA-MB-231). Analysis of m-$CaCO_3$ penetration into the breast tumor showed a limited reduction in T_2, suggesting less uptake than observed previously in the HT1080 fibrosarcoma model (Figure 2C vs Figure 3A). Differential penetration and kinetics were observed depending on the size of the tumor. To determine the tumor pH, we used the acidoCEST-MRI method. Pioneered by the Pagel group, acidoCEST detects the differential rate of proton transfer of the amine group of iopamidol under different pH conditions, creating two separate peaks on MRI [28]. By measuring the ratio of the intensity of the two peaks, we can estimate the pH *in vivo* [29]. We used nano-$CaCO_3$ instead of m-$CaCO_3$ to prevent confounding signals from the magnetite and iopamidol imaging agents. We found that the tumors exhibited an average extracellular pH (pH_e) of 6.8 before nano-$CaCO_3$ injection, which increased to 7.04 before dropping to 6.54 at 24 h postinjection, ($p < 0.054$;

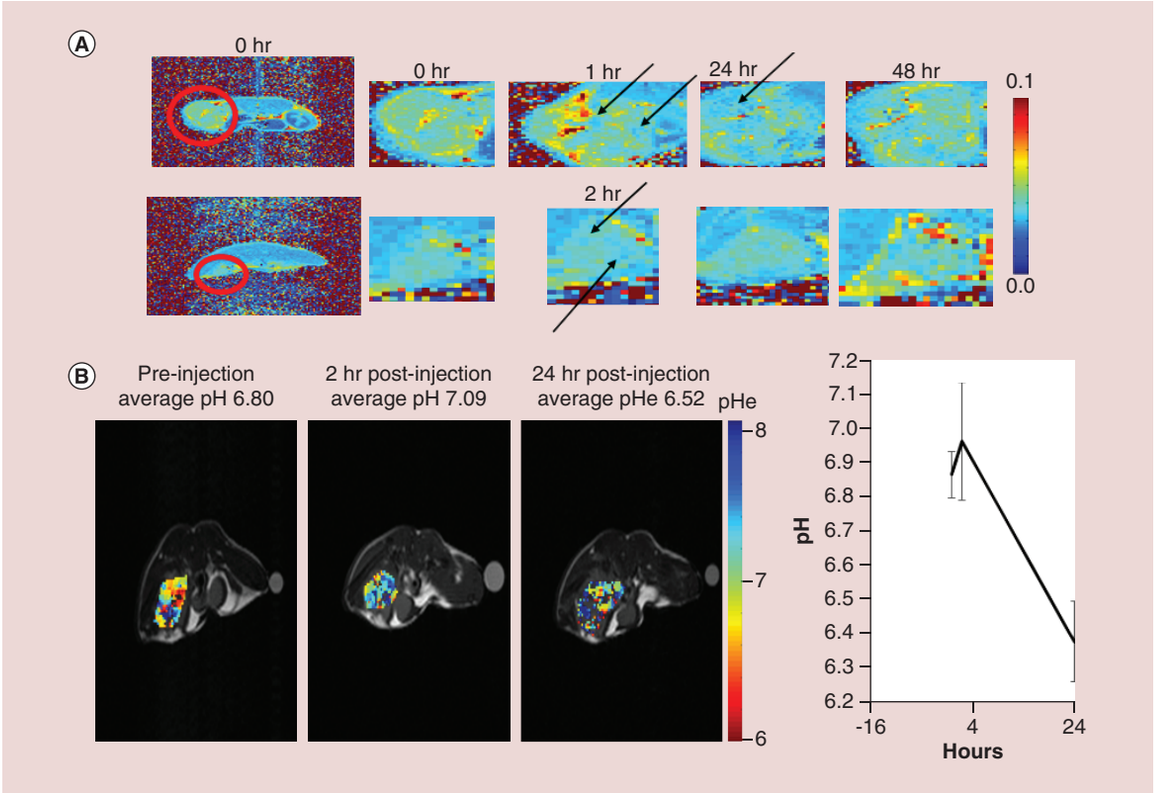

Figure 3. Magnetite $CaCO_3$ measurement in breast cancer model and subsequent effect on pH. (A) Measurement of magnetite $CaCO_3$ distribution in the cross-section of mice with an MDA-MB-231 xenograft. Heat map shows T_2 signal. Red circle indicates tumor, with enlarged cutouts to the right. Black arrows show drops in T_2 attributed to the magnetite core, with differential penetration in large and small tumors, and distribution peaking somewhere between 1 and 24 h dependent on size. Representative images (n = 3 mice, one experiment). **(B)** MRI-based pH measurement in a breast cancer MDA MB-231 model treated with $CaCO_3$ nanoparticle. Left, representative images, heat map shows pH. Right, average tumor pH (n = 3 mice, one experiment).

Figure 3B). This result indicates that the clearance of nano-$CaCO_3$ from the tumor region at 24 h decreased the pH to a level lower than baseline.

Continuous infusion of nano-$CaCO_3$ decreases lung metastasis

Rebound of the acidic environment of tumors after clearance of nano-$CaCO_3$ suggests that continuous infusion of particles could maintain the pH above 7 and potentially induce a sustained inhibition in tumor metastasis and growth. As current osmotic pumps for infusion in murine models only last 30 days, we opted to use the aggressively metastasizing 4T1luc-GFP orthotopic breast cancer model. Mice were implanted with an osmotic pump containing nano-$CaCO_3$ and cypate, a near-infrared (NIR) dye [30], followed by mammary fat pad implantation of the tumor cells. Metastasis to the lung was measured by transcutaneous bioluminescence. Planar NIR fluorescence imaging suggested that most of the materials were released by day 19 (Figure 4A). The residual NIR fluorescence on day 19 is from the pump implanted in the dorsum of the mice with a catheter into their internal jugular vein. Although nano-$CaCO_3$ treatment nearly doubled the time to metastasis, the long-term survival benefit was not statistically significant (Figure 4B; p = 0.19, Kaplan–Meier log rank test), indicating that nano-$CaCO_3$ may act by inhibiting extravasation. Next, we explored the feasibility of using nano-$CaCO_3$ to reduce metastatic tumor growth in the lungs due to extravasation of circulating tumor cells. The nano-$CaCO_3$ infusion inhibited metastatic growth of 4T1luc-GFP cells in the lungs of mice after intravenous injection (Figure 4C & D). There was a strong trend in metastasis inhibition in the iv. infusion model (p = 0.0576, two-way Analysis of variance [ANOVA], repeated measures). There was a statistically significant difference in growth at day 2 postinjection (p = 0.02, 2-tailed unpaired t-test), but no statistically significant differences were found on other days (p = 0.16, 0.46, 0.22, 0.16,

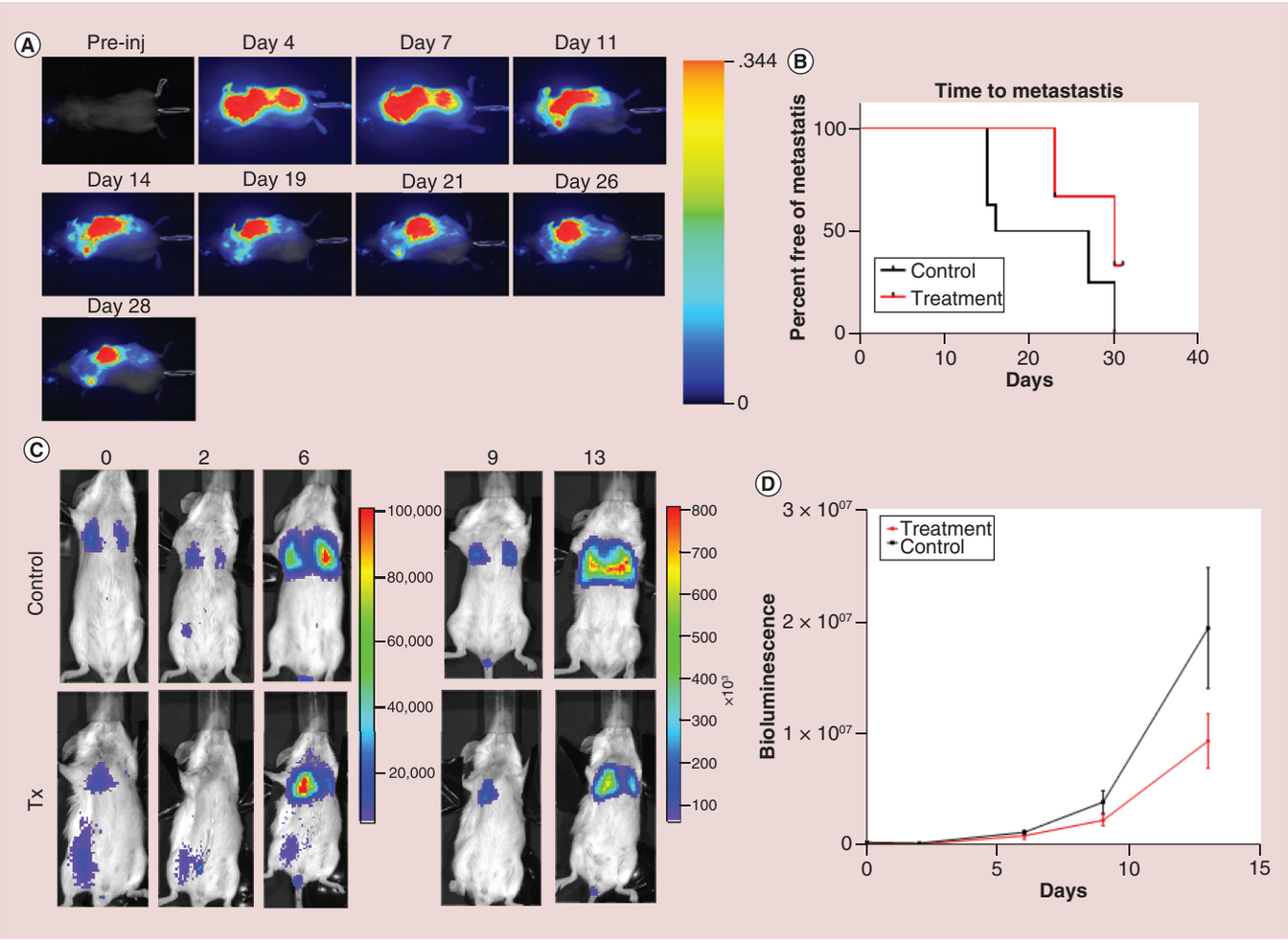

Figure 4. Proof-of-concept continuous infusion of nano-$CaCO_3$ may inhibit metastasis. Mice were implanted with osmotic infusion pumps containing nano-$CaCO_3$ nanoparticle and near-infrared dye cypate (treatment) or left untreated (control). **(A)** Near-infrared fluorescence of cypate as evidence of nano-$CaCO_3$ release over time, heat map shows near-infrared signal. **(B)** Mice were implanted with orthotopic 4T1luc tumors and metastasis from orthotopic site to the lungs was tracked by bioluminescence. Time to metastasis is graphed, with control in black (n = 8, two experiments) and treatment in red (n = 3, one experiment). In **(C–D)**, tumor cells were introduced via – tail vein injection, and tumor seeding and growth was tracked by bioluminescence over time (n = 3/group, one experiment). **(C)** Representative images of control and nano-$CaCO_3$ treated mice. Scale is radiance (photons/sec/cm^2/steradian). Note, bioluminescence outside of the lung region in the treated group is attributed to the infusion pump itself as described by the manufacturer. **(D)** Quantification of lung bioluminescence in photons/s. Error bars are standard error of the mean [31].
Nano-$CaCO_3$: $CaCO_3$ nanoparticles.

at day 0, 6, 9, 13 postinjection, respectively, 2-tailed unpaired t-test). The control experiment ran in parallel and had to be terminated early due to weight loss in the control animals. Thus, continuous infusion of nano-$CaCO_3$ limited extravasation and metastasis of tumor cells.

Evaluating toxicity of $CaCO_3$ nanoparticles *in vitro* & *in vivo*

Toxicity of nanoparticles can arise from several factors, including size, charge, constituents and metabolites. As such, we characterized the toxicity of nano-$CaCO_3$. Data analysis showed that the particles did not exhibit specific cytotoxicity on HT1080 cells treated with up to 1.20 mg/ml *in vitro* (Figure 5A). For *in vivo* studies, rats were used in order to obtain sufficient blood samples for analysis at multiple time points. Nano-$CaCO_3$-treated rats did not exhibit significant changes in organ weights, blood chemistries and blood counts up to 24 h after 25 mg/kg nano-$CaCO_3$ injection (Figure 5B–D). A slight increase in blood urea nitrogen was observed, which is not likely a toxic effect because there was no concurrent increase in the creatinine or liver enzymes. A single animal exhibited

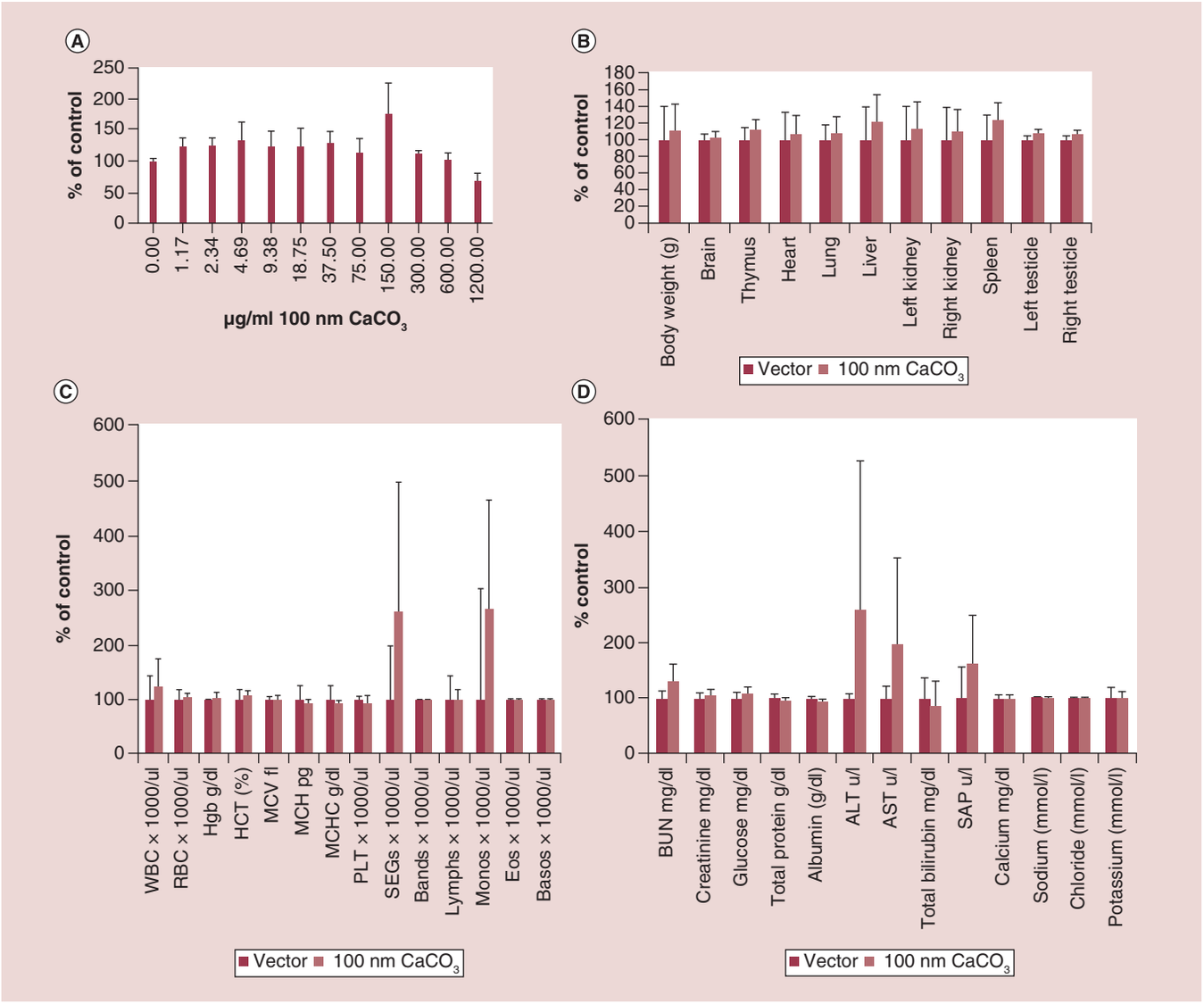

Figure 5. $CaCO_3$ nanoparticle does not show toxicity *in vitro* or *in vivo*. (A) Cytotoxicity of $CaCO_3$ nanoparticles as measured by the percentage of HT1080 cell surviving when incubated with 100 nm CaO_3 nanoparticles in standard pH 7.4 media (n = 4 technical replicates, one experiment). For **(B–D)**, rats were injected with 30 mg/ml at 25 mg/kg CaO_3 nanoparticles or vector alone (n = 3/group, one experiment). **(B)** Organ weights with solvent versus 100 nm CaO_3 nanoparticles. **(C)** Complete blood count. **(D)** Serum biomarker values. MCH: Mean cell hemoglobin; MCV: Mean corpuscular volume; RBC: Red blood cell; WBC: White blood cell.

an increase in neutrophil counts as well as liver enzyme levels (ALT and AST) that were confounded by the presence of pneumonia in the animal (Figure 5C–D).

Discussion

The ability to visualize $CaCO_3$ by impregnating magnetite nanoparticles into the existing nanoparticle formulations allows for the noninvasive assessment of the *in vivo* assessment of the biodistribution of this traceless material in animal models of cancer. The magnetite is uniformly distributed across the particle and remains in the particle even during dissolution, allowing for a better approximation of the location of the entire particle. Despite the different synthesis methods used to prepare both m-$CaCO_3$ and nano-$CaCO_3$, the nanoparticles exhibited similar stability in different solvents. Because m-$CaCO_3$ maintains the same vaterite-like crystal properties as shown by XRD, it may have exhibited the same surface properties as nano-$CaCO_3$. By maintaining similar surface properties, m-$CaCO_3$ can be used to predict the behavior of the non-signaling nano-$CaCO_3$ under similar *in vivo* conditions.

MRI of m-$CaCO_3$ clearly shows differing distributions between the fibrosarcoma and breast cancer models, a diversity suspected to also exist *in vivo* clinically. These differences point to the importance of determining the biodistribution of nanoparticles in different tumor types for therapeutic optimization. The noninvasiveness of MRI-based tracking of the particles biodistribution makes it ideal for both preclinical optimization and eventual *in vivo* human studies.

Additionally, the combination of MRI for m-$CaCO_3$ distribution and acidoCEST-MRI or FDG-PET for metabolic changes permits fully noninvasive and clinically translatable assessment of nano-$CaCO_3$ efficacy *in vivo*. Previous studies on nano-$CaCO_3$ used invasive methods to measure pH changes, which detected pH increase but failed over time due to acidity induced by pressure necrosis. Noninvasive pH measurements remain difficult because of limited pH sensitivity above 7 for many probes. However, noninvasive techniques such as acidoCEST imaging are useful to measure any potential drops in pH *in vivo*, including a return to pretreatment acidic pHe value. To map the metabolic reprogramming of the tumor, FDG-PET can be used to monitor glucose uptake, which can be overlaid with MRI data showing m-$CaCO_3$ biodistribution from the same individual. With these multiple imaging modalities, we could perform parallel experiments to correlate biodistribution of m-$CaCO_3$ and changes in pHe and glucose uptake *in vivo* and provide complementary information on how these particles modulate the pHe of tumors in multiple tumor models.

Biodistribution data using m-$CaCO_3$ was able to shed light on previous findings using nano-$CaCO_3$. We had previously demonstrated a tumor-static effect of nano-$CaCO_3$ administration and pHe increase in an HT1080 fibrosarcoma model [12]. We found that daily nano-$CaCO_3$ injections were required for therapeutic efficacy, and tumor growth resumed after nano-$CaCO_3$ injections were stopped. These effects may be explained by MRI imaging showing the majority of the nanoparticles were cleared within in 24 h. Thus, continuous retention of nano-$CaCO_3$ is likely required to prevent tumor growth, which matches with the results we found here using continuous infusion to prevent metastasis. Understanding the dissolution of these particles will require determination of the elemental composition of these nanoparticles over time. This information could further elucidate the release kinetics of calcium and iron from the m-$CaCO_3$.

Our results from the FDG-PET and acidoCEST studies appear to demonstrate tumor metabolic reprogramming. In the HT1080 fibrosarcoma model, we found reduced FDG uptake in the tumor at 24 h, indicating nano-$CaCO_3$ exposure may have affected the tumor's reliance on Warburg metabolism. Conversely, nano-$CaCO_3$ produced a drop in tumor pH after nanoparticle clearance in the MDA-MB-231 model. A previous study using a pH electrode showed that nano-$CaCO_3$ can increase the pHe of tumors from 6.8 to 7.4 over the course of several hours [12]. However, in this study, noninvasive imaging using acidoCEST-MRI detected a drop in pHe to 6.54 at 24 h post-treatment, which is below the average pH before injection. This finding suggests that $CaCO_3$ induces a biological response from tumor cells that overcompensates for the initial alkalization, resulting in a lower pHe after the buffering nanoparticles are cleared from the tumor. This overcompensation suggests that tumors tightly and actively maintain acidic pHe, indicating that this process is not simply a spontaneous byproduct of lactic acid accumulation. This overcompensation confirms the need to sustain local nano-$CaCO_3$ concentration in tumor microenvironment for effective inhibition of cancer progression and metastasis.

To combat this overcompensation, we explored the use of continuous infusion of nano-$CaCO_3$ in a metastasis model. Increasing pH has been demonstrated to inhibit both metastasis and cancer cell extravasation in tumor models [11]. In our study, we found that the release of the majority of nanoparticles over 19 days correlated with lower levels of metastasis to the lung. A previous report showed a similar trend of metastasis inhibition when systemic pH was raised with sodium carbonate [11]. In contrast, our nanoparticle approach inhibited extravasation at approximately 30,000-fold lower dose than the previously reported required oral dosing of sodium bicarbonate. More study, however, is required to confirm that nano-$CaCO_3$ can indeed limit metastasis, ideally utilizing a pump with longer duration in larger animals, and with concurrent long term placebo controls.

Alteration of systemic acid/base status outside physiological normal pH (7.2–7.4) is known to induce pathological effects [12]. Therefore, we evaluated the potential toxicity of nano-$CaCO_3$ in rats, which were used to obtain sufficient blood samples for analysis. The results from the rat studies suggest minimal acute toxicity, except one rat that appeared to suffer from pneumonitis of unknown etiology, which showed increased liver enzymes and neutrophil counts. Nevertheless, further studies on the potential for long-term toxicity from multiple doses or continuous infusion with larger cohort will be required before human application.

Although the results of this study are promising, there are limitations to m-$CaCO_3$ and the available methods for detecting its effects. Although magnetite allows for MRI-based noninvasive imaging, measurements are not

quantitative and have low sensitivity. We were not able to obtain a longitudinal quantification of nanoparticle distribution because of technical constraints that include hypothermia caused by prolonged anesthesia. Future studies will explore alternative ways to determine quantitatively the pharmacokinetics of m-$CaCO_3$ in the kidney and liver for longer durations than presented here. As such, the inability to estimate what concentration of nano-$CaCO_3$ accumulates in tissues or at what time after injection it is eliminated as opposed to when the amount drops below signal visibility, prevents accurate estimation of the total nano-$CaCO_3$ effect on pHe. In addition, acidoCEST allows noninvasive monitoring of the effect of $CaCO_3$ on pHe, but has limited ability to detect pH above 7, confining its use to pretreatment or postclearance than during nano-$CaCO_3$ therapy. A limitation of acidoCEST-MRI is that it does not allow, at the time of experimentation, the capability for continuous monitoring or extended daily time point imaging to avoid deleterious effects on mouse welfare, which limited the exploration of pH acidification. Future studies will continue to explore this question of acidification at longer time points as new and user-friendly pH measurement methods become available.

Conclusion

We developed m-$CaCO_3$ for MRI and used it to determine nano-$CaCO_3$ biodistribution noninvasively in two separate solid tumor types. A combination of acidoCEST-MRI and FDG-PET allowed us to assess the effects of nano-$CaCO_3$ treatment. We discovered that nano-$CaCO_3$-induced pH changes can cause tumors to reprogram their metabolic function, as evidenced by changes in pH and 18-FDG uptake in MDA-MB-231 and HT1080 tumors, respectively. Based on these results, several directions are currently under investigation with the particles, including methods to increase targeting and retention of the nano-$CaCO_3$ at the tumor region and understanding how these particles stimulate cellular reprogramming. Given the substantial literature surrounding chemotherapy sensitivity to pH, the ability of nano-$CaCO_3$ to increase and decrease tumor pHe may be used to optimize the retention and potentiation of a wide range of existing therapies [32]. Rat toxicity data suggest minimal side effects of treatment, enabling future translation to larger animal studies. The combination of this novel material synthesis and biological analysis offers the first evidence of tumor reprogramming by extracellular environment change by a nanoparticle with multiple possible applications in cancer therapy.

Summary points

- Incorporation of magnetite into $CaCO_3$ nanoparticle (nano-$CaCO_3$) produces an MRI imaging agent that is capable of assessing the nanoparticles biodistribution and pH modulation noninvasively.
- Magnetite $CaCO_3$ has similar surface and solubility properties as nano-$CaCO_3$ in *in vivo*.
- Nano-$CaCO_3$ induces a transient pH increase in the tumor microenvironment and downregulation of radiolabeled glucose uptake in tumors.
- After clearance, nano-$CaCO_3$ also leads to an overcompensation of acidity by the tumor, demonstrating a metabolic reprogramming response to extracellular pH change.
- Continuous infusion of nano-$CaCO_3$ could prevent rapid clearance and inhibit tumor metastasis.
- Nano-$CaCO_3$ is biocompatible, exhibiting minimal toxic effects *in vitro* and *in vivo*.
- Differences in tumor response to nano-$CaCO_3$ suggest a need to optimize dosage, administration protocol and molecularly targeted delivery for different cancer types.
- Incorporation of magnetite into carbonates-based nanoparticles provides an opportunity to intelligently design diverse nanometal carbonates and noninvasively determine their biodistribution, therapeutic effects and pH modulation of tissues.

Supplementary data

To view the supplementary data that accompany this paper please visit the journal website at: www.futuremedicine.com/doi/full/10.2217/nnm-2018-0302

Financial & competing interests disclosure

A Som was supported by the NCI F30CA189435-03 and NIH training Grant Number T32 GM07200. R Raliya, L Habimana-Griffin and N Reed were supported by NIH-NCI U54CA199092. AY Mah-Som was supported by NIAID 1F30AI129110 and NIH training Grant Number T32 GM07200. WJ Akers was supported by NCI R50 CA211481. JL Prior was supported by NIH P50 CA094056 (Molecular Imaging Center) and NCI P30 CA091842 (Siteman Cancer Center Small Animal Cancer Imaging shared resource). The

study was funded in part by grants from the National Institutes of Health (U54 CA199092, R01 EB021048, R01 CA171651, P50 CA094056, P30 CA091842, S10 OD016237, S10 RR031625 and S10 OD020129), Department of Defense Breast Cancer Research Program (W81XWH-16-1-0286), and the Alvin J Siteman Cancer Research Fund (11-FY16-01). The authors have no other relevant affiliations or financial involvement with any organization or entity with a financial interest in or financial conflict with the subject matter or materials discussed in the manuscript apart from those disclosed.

No writing assistance was utilized in the production of this manuscript.

Ethical conduct of research

All animal studies were conducted in compliance with Washington University and Arizona University Animal Welfare Committees' requirements for the care and use of laboratory animals in research. The authors state that they have obtained appropriate institutional review board approval or have followed the principles outlined in the Declaration of Helsinki for all human or animal experimental investigations.

Acknowledgments

The authors would like to acknowledge D Hathi for help with the MR analysis, as well as the help by the staff of the Mallinckrodt Institute of Radiology microPET Facility and SC Greco of the Washington University in St Louis Division of Comparative Medicine for aid in toxicity studies.

References

Papers of special note have been highlighted as: • of interest; •• of considerable interest

1. Cavaletti G, Bogliun G, Marzorati L *et al.* Grading of chemotherapy-induced peripheral neurotoxicity using the Total Neuropathy Scale. *Neurology* 61(9), 1297–1300 (2003).
2. Barnett GC, West CM, Dunning AM *et al.* Normal tissue reactions to radiotherapy: towards tailoring treatment dose by genotype. *Nat. Rev. Cancer* 9(2), 134–142 (2009).
3. Ojugo AS, McSheehy PM, McIntyre DJ *et al.* Measurement of extracellular pH of solid tumors in mice by MR Spectroscopy. Comparison of exogenous 19^F and 31^P probes. *NMR in Biomed.* 12, 495–504 (1999).
4. Zhang X, Lin Y, Gillies RJ. Tumor pH and its measurement. *J. Nucl. Med.* 51(8), 1167–1170 (2010).
5. Pietras K, Ostman A. Hallmarks of cancer: interactions with the tumor stroma. *Exp. Cell Res.* 316(8), 1324–1331 (2010).
6. Hanahan D, Weinberg RA. Hallmarks of cancer: the next generation. *Cell* 144(5), 646–674 (2011).
7. Ueno Y, Futagawa H, Takagi Y, Ueno A, Mizushima Y. Drug-incorporating calcium carbonate nanoparticles for a new delivery system. *J. Control. Release* 103(1), 93–98 (2005).
8. Lee ES, Shin HJ, Na K, Bae YH. Poly(l-histidine)–PEG block copolymer micelles and pH-induced destabilization. *J. Control. Release* 90(3), 363–374 (2003).
9. Torchilin VP. Cell penetrating peptide-modified pharmaceutical nanocarriers for intracellular drug and gene delivery. *Biopolymers* 90(5), 604–610 (2008).
10. Bellone M, Calcinotto A, Filipazzi P, De Milito A, Fais S, Rivoltini L. The acidity of the tumor microenvironment is a mechanism of immune escape that can be overcome by proton pump inhibitors. *Oncoimmunology* 2(1), e22058 (2013).
11. Robey IF, Baggett BK, Kirkpatrick ND *et al.* Bicarbonate increases tumor pH and inhibits spontaneous metastases. *Cancer Res.* 69(6), 2260–2268 (2009).

•• **Robey *et. al.*'s work on bicarbonate inhibiting metastasis was one of the first to demonstrate that pH in the extracellular environment is more than a byproduct of dysregulated glycolysis and serves the reader as a base on which much pH modulation work was done.**

12. Som A, Raliya R, Tian L *et al.* Monodispersed calcium carbonate nanoparticles modulate local extracellular pH and inhibit tumor growth *in vivo*. *Nanoscale* (8(25), 12639–12647 (2015).

•• **Our work here first showed how to synthesize, stabilize and use therapeutically nano-$CaCO_3$ and is a good connected article.**

13. Lee ES, Gao Z, Bae YH. Recent progress in tumor pH targeting nanotechnology. *J. Control. Rel.* 132(3), 164–170 (2008).
14. Thews O, Gassner B, Kelleher DK, Schwerdt G, Gekle M. Impact of extracellular acidity on the activity of P-glycoprotein and the cytotoxicity of chemotherapeutic drugs. *Neoplasia* 8(2), 143–152 (2006).
15. McIntyre A, Patiar S, Wigfield S *et al.* Carbonic anhydrase IX promotes tumor growth and necrosis *in vivo* and inhibition enhances anti-VEGF therapy. *Clin. Cancer Res.* 18(11), 3100–3111 (2012).
16. Vaupel P. Tumor microenvironmental physiology and its implications for radiation oncology. *Semin. Radiat. Oncol.* 14(3), 198–206 (2004).

17. Peng H, Li K, Wang T *et al.* Preparation of hierarchical mesoporous $CaCO_3$ by a facile binary solvent approach as anticancer drug carrier for etoposide. *Nano Express* (8), 321 (2013).

18. Lauth V, Maas M, Rezwan K. An evaluation of colloidal and crystalline properties of $CaCO_3$ nanoparticles for biological applications. *Mater. Sci. Eng. C Mater. Biol. Appl.* 78, 305–314 (2017).

- **The work by Lauth shows a detailed understanding of $CaCO_3$ crystalline properties and interaction *in vivo*.**

19. Qi C, Lin J, Fu LH, Huang P. Calcium-based biomaterials for diagnosis, treatment, and theranostics. *Chem. Soc. Rev.* 47(2), 357–403 (2018).

20. Raliya R, Som A, Shetty N, Reed N, Achilefu S, Biswas P. Nano-antacids enhance pH neutralization beyond their bulk counterparts: synthesis and characterization. *RSC Adv.* 6(59), 54331–54335 (2016).

21. Rosenblum LT, Kosaka N, Mitsunaga M, Choyke PL, Kobayashi H. *In vivo* molecular imaging using nanomaterials: general *in vivo* characteristics of nano-sized reagents and applications for cancer diagnosis. *Mol. Membr. Biol.* 27(7), 274–285 (2010).

22. Shin TH, Choi Y, Kim S, Cheon J. Recent advances in magnetic nanoparticle-based multi-modal imaging. *Chem. Soc. Rrv.* 44(14), 4501–4516 (2015).

23. Li W, Liu D, Wu J, Kim C, Fortner JD. Aqueous aggregation and surface deposition processes of engineered superparamagnetic iron oxide nanoparticles for environmental applications. *Environ. Sci. Technol.* 48(20), 11892–11900 (2014).

24. Chen LQ, Howison CM, Spier C *et al.* Assessment of carbonic anhydrase IX expression and extracellular pH in B-cell lymphoma cell line models. *Leuk. Lymphoma* 56(5), 1432–1439 (2015).

25. Chen LQ, Randtke EA, Jones KM, Moon BF, Howison CM, Pagel MD. Evaluations of tumor acidosis within *in vivo* tumor models using parametric maps generated with acido-CEST MRI. *Mol. Imaging Biol.* 17(4), 488–496 (2015).

- **This work goes through how acido-CEST MRI can be used to measure pH noninvasively and is a critical novel technique for analysis for noninvasive extracellular pH measurement.**

26. Akhenblit PJ, Hanke NT, Gill A *et al.* Assessing metabolic changes in response to mTOR inhibition in a mantle cell lymphoma xenograft model using Acido-CEST MRI. *Mol. Imaging* 15 doi: 10.1177/1536012116645439 (2016).

27. Vichai V, Kirtikara K. Sulforhodamine B colorimetric assay for cytotoxicity screening. *Nat. Protoc.* 1(3), 1112–1116 (2006).

28. Sheth VR, Li Y, Chen LQ, Howison CM, Flask CA, Pagel MD. Measuring *in vivo* tumor pHe with CEST-FISP MRI. *Magn. Reson. Med.* 67(3), 760–768 (2012).

29. Chen LQ, Howison CM, Jeffery JJ, Robey IF, Kuo PH, Pagel MD. Evaluations of extracellular pH within *in vivo* tumors using acido-CEST MRI. *Magn. Reson. Med.* 72(5), 1408–1417 (2014).

30. Achilefu S, Dorshow RB, Bugaj JE, Rajagopalan R. Novel receptor-targeted fluorescent contrast agents for *in vivo* tumor imaging. *Invest. Radiol.* 35(8), 479–485 (2000).

31. Alzet. Alzet Technical Sheet 1.1, *in vivo* bioluminescence imaging using alzet osmotic pumps. www.alzet.com/resources/documents/BLITechSheet_applications.pdf

32. Stubbs M, McSheehy PM, Griffiths JR, Bashford CL. Causes and consequences of tumour acidity and implications for treatment. *Mol. Med. Today* 6, 15–19 (2000).